THE JOURNAL OF PHYSICAL CHEMISTRY A
A JOURNAL OF THE AMERICAN CHEMICAL SOCIETY

pubs.acs.org/JPCA Article

Calculation of Solid–Fluid Interfacial Free Energy with Consideration of Solid Deformation by Molecular Dynamics Simulations

Tianhao Wu and Abbas Firoozabadi*

Cite This: J. Phys. Chem. A 2021, 125, 5841–5848 Read Online

ACCESS | Metrics & More | Article Recommendations | Supporting Information

ABSTRACT: Fluid–fluid interfacial free energy can be measured accurately and can also be calculated from molecular simulations. However, it is challenging to measure solid–fluid interfacial free energy directly. Accurate computation has not yet been advanced by molecular simulations. In this study, we derive working expressions for estimating solid–fluid interfacial free energy based on the free-energy perturbation method with consideration of solid deformation. A Lennard–Jones solid–fluid system is simulated. Our derivations indicate that the effect of solid deformation is pronounced on solid–fluid interfacial free energy, and the results may be significantly different from the conventional test area method. Our results reveal that the contribution of the solid deformation highly depends on the stress conditions in the solid, which can be either positive or negative. Adsorption of fluids onto the solid surface has a significant effect on interfacial free energy. In weak adsorption, the interfacial free energy is close to the solid–vacuum surface free energy. Strong adsorption results in a significant reduction in interfacial free energy.

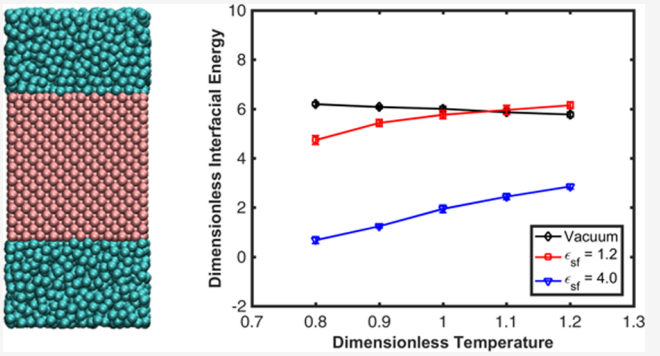

1. INTRODUCTION

Interfacial free energy density is a major topic in science and industry. In gas–liquid interfaces, the surface free energy is often referred to as surface tension. In liquid–liquid interfaces, both interfacial free energy density and interfacial tension refer to the same interfacial property. There are various methods to measure fluid–fluid interfacial free energy.[1] In fluid–solid interfaces, the measurement of the interfacial tension is much more complicated, and only indirect methods have been used. These include cleavage tests for mica–water, solubility tests for quartz–water based on the Freundlich–Ostwald equation, and contact angle measurements based on Young's equation.[2−4]

Knowledge of solid–fluid interfacial free energy is critical to many engineering problems. Hydraulic fracturing is a key technology in shale oil and gas development. Different fracturing fluids such as H_2O, CO_2, and N_2 may lead to different fracturing pressures, fracture intensities, and shapes of fractures.[5−9] The mechanisms of fracturing by different fluids are not well understood, especially for CO_2.[10−17] In fracturing simulations, fracture toughness defines a material's ability to resist fracture propagation. The toughness is often characterized by the critical energy release rate G_c, which is defined as the critical stored strain energy released per unit crack area at the moment of fracture extension in elastic materials.[18,19] G_c is a key parameter in fracture propagation. The phase-field method for numerical simulations of hydraulic fracturing is based on G_c.[20,21] The critical energy release rate can be estimated directly from surface free-energy density. Griffith[22,23] proposed the theory of rock failure based on surface free-energy density γ_s as $G_c = 2\gamma_s$. Irwin[19,24,25] extended Griffith's theory by considering the energy needed to create a damaged zone of plastic deformation ahead of the crack tip. Irwin proposed that $G_c = 2(\gamma_s + \gamma_p)$, where γ_p is the plastic work per unit area of the surface created.[18] We have recently confirmed Irwin's theory from molecular simulations of kerogen failure.[18] For a solid in contact with a fluid, G_c is related to solid–fluid interfacial free-energy density γ_{sf}.

As mentioned above, the fluid–fluid interfacial free energy can be estimated by various methods, while the method for the solid–fluid interface is still under debate. In molecular simulations, fluid–fluid interfacial free energy can be computed using the Kirkwood–Buff relation based on tensorial components of pressure.[26] An isobaric–isothermal–isointerfacial area ensemble, referred to as the Np_zT ensemble, is often applied.[27] In a planar interface perpendicular to the z-axis, the interfacial free energy is given by

Received: January 26, 2021
Revised: June 9, 2021
Published: June 28, 2021

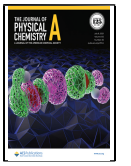

$$\gamma = \frac{L_z}{2}(\langle p_N \rangle - \langle p_T \rangle) \quad (1)$$

where p_N and p_T are the normal and tangential components of pressure and L_z is the dimension of the domain in the z-direction.

There is an alternative approach to compute interfacial free-energy density based on interfacial thermodynamics. The thermodynamic relation for the change in Helmholtz free energy F in fluid−fluid systems is given by

$$dF = -SdT - pdV + \sum_i \mu_i dN_i + \gamma dA \quad (2)$$

where S is entropy, T is temperature, p is pressure, V is volume, μ_i is the chemical potential of component i, N_i is the number of particles of species i, γ is interfacial free-energy density, and A is the interfacial area. At constant temperature, volume, and number of particles, the interfacial free-energy density can be estimated by

$$\gamma = \left(\frac{\partial F}{\partial A}\right)_{N_i,V,T} \quad (3)$$

This method relies on accurate estimation of the free energies from two different simulations with different interfacial areas, which is challenging for many complex molecular systems. The alternative is the test area method proposed by Gloor et al.,[28] using which free-energy perturbations are performed instead of calculating the free-energy difference. The test area method is used to perform a perturbation of the surface area at constant volume, in which the overall properties of the reference system persist (see Figure 1). The change in Helmholtz free energy

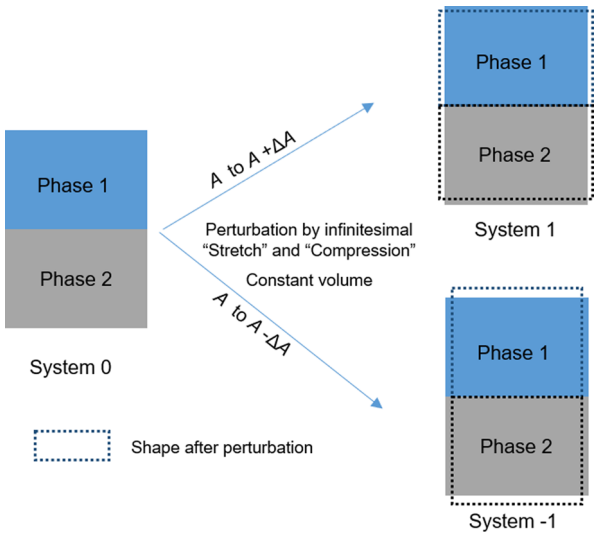

Figure 1. Sketch of the test area method. System 0 corresponds to the condition before perturbation. Systems 1 and −1 correspond to the conditions after the infinitesimal stretch and compression, respectively.

between the initial state 0 and the perturbed state 1 is given as[28,29]

$$\Delta F_{0\to 1} = -k_B T \ln\left\langle \exp\left(-\frac{\Delta U}{k_B T}\right)\right\rangle \quad (4)$$

where k_B is the Boltzmann constant and ΔU is the change of potential energy due to the perturbation. Based on eq 3, the interfacial free energy can be estimated by

$$\gamma = \left(\frac{\partial F}{\partial A}\right)_{N_i,V,T} = \lim_{\Delta A\to 0}\left(\frac{\Delta F}{\Delta A}\right)_{N_i,V,T} = -\frac{k_B T}{\Delta A}\ln\left\langle \exp\left(-\frac{\Delta U}{k_B T}\right)\right\rangle \quad (5)$$

To increase accuracy, the central finite difference scheme has been suggested based on two separate perturbations, including positive (stretch) and negative (compression) perturbations of the interfacial area.[28] The interfacial energy is then obtained from

$$\gamma = \frac{F(A+\Delta A) - F(A-\Delta A)}{2\Delta A} = \frac{\Delta F_{0\to 1} - \Delta F_{0\to -1}}{2\Delta A} \quad (6)$$

Other methods in the literature are proposed for the estimation of the difference of solid−fluid interfacial free energy ($\Delta\gamma$) between different systems instead of the absolute value of interfacial energy. These include the phantom wall method and the contact angle method. In the phantom wall method, a structureless wall is used to push the fluid away from the solid phase, in which the phantom wall only interacts with the fluid molecules.[4,30] The phantom wall method provides the difference only in interfacial free energy between solid−fluid and phantom wall−fluid or solid−two different fluids. The absolute value of interfacial free energy can be estimated only if the surface free energy of the solid phase is known. In addition, similar methods based on thermodynamic integration are widely used to obtain interfacial free energy or the relative change, such as the cleaving wall method, multischeme thermodynamic integration, and dry surface method.[31−34] In a three-phase system, the interfacial free energy difference $\Delta\gamma$ can also be calculated based on the contact angle from direct simulations of droplets on solid surfaces.[4,35] The interfacial free energy difference $\Delta\gamma$ is estimated based on Young's equation as

$$\Delta\gamma = \gamma_{sf_2} - \gamma_{sf_1} = \gamma_{f_{1,2}}\cos\theta \quad (7)$$

where θ is the contact angle, γ_{sf_1}, γ_{sf_2}, and $\gamma_{f_{1,2}}$ are the interfacial free energies of solid−fluid 1, solid−fluid 2, and fluid 1−fluid 2, respectively. The validity of eq 7 is under debate at the molecular scale.[4]

Some authors have used the test area method for the calculation of solid−fluid interfaces without consideration of the solid deformation.[36−38] The stress in solids can be very sensitive to strain, even for small perturbations, depending on elastic modulus. This effect may have a pronounced influence on the relationship between interfacial free energy and free energy change and may lead to significant errors.

In this work, we introduce a formulation that accounts for solid deformation based on the free energy perturbation method for the calculation of solid−fluid interfacial energy. The method is verified using the Lennard−Jones (LJ) molecular description. We analyze the contribution of solid deformation to the conventional test area method. The effects of temperature, pressure, and adsorption on solid−fluid interfacial free energy are investigated.

https://doi.org/10.1021/acs.jpca.1c00735
J. Phys. Chem. A 2021, 125, 5841−5848

2. METHODOLOGY

2.1. Free-Energy Perturbation Method. Our proposed free-energy perturbation method is based on the test area method with consideration of solid deformation. The derivation is provided in the Supporting Information.

In an isotropic and homogeneous body, the change in Helmholtz free energy from a perturbation in the surface area, temperature, and strain (of a closed system) is given by

$$dF = -SdT + \gamma dA + V\sum_i\sum_j \sigma_{ij}d\varepsilon_{ij} \tag{8}$$

where σ_{ij} and ε_{ij} are components of the stress and strain tensor, respectively, and i and j are plane indices. Tension is defined as positive. One can perform an infinitesimal perturbation of a pure shear process in a slab with two interfaces at a constant temperature. The volume of the slab is kept constant, but the shape is changed when we implement the perturbation on the surface area. For such a process, eq 8 becomes (see the Supporting Information)

$$dF = 2\gamma dA + \frac{EL_z}{1+\nu}\left[\frac{1}{2}(\varepsilon_{xx}+\varepsilon_{yy}) - \varepsilon_{zz}\right]dA \tag{9}$$

where E is Young's modulus, ν is Poisson's ratio, L_z is the thickness of the solid slab in the z-direction, and $V = AL_z$. The factor 2 in the first term represents a slab's two surfaces. Equation 4 is also applicable for the change in Helmholtz free energy density from the perturbation. Combining eqs 4 and 9 gives

$$\gamma = -\frac{k_BT}{2\Delta A}\ln\left\langle \exp\left(-\frac{\Delta U}{k_BT}\right)\right\rangle - \frac{EL_z}{2(1+\nu)}\left[\frac{1}{2}(\varepsilon_{xx}+\varepsilon_{yy}) - \varepsilon_{zz}\right] \tag{10}$$

Equations 8 to 10 are general for both fluids and solids. In fluids, the deformation corresponds to hydrostatic expansion or compression, and the second term on the right side is zero. In our evaluation, the central finite difference is used to increase accuracy. The two separate perturbations include stretch (positive) and compression (negative) of the interfacial area, which correspond to the potential energy change of ΔU^+ and ΔU^-, respectively. The interfacial free energy density of a solid−fluid system is then given by

$$\gamma_{sf} = -\frac{k_BT}{4\Delta A}\left[\ln\left\langle \exp\left(-\frac{\Delta U^+}{k_BT}\right)\right\rangle - \ln\left\langle \exp\left(-\frac{\Delta U^-}{k_BT}\right)\right\rangle\right] - \frac{EL_{z,s}}{2(1+\nu)}\left[\frac{1}{2}(\varepsilon_{xx}+\varepsilon_{yy}) - \varepsilon_{zz}\right] \tag{11}$$

where the subscripts s and f denote the solid and fluid phases, respectively. The working expression in terms of the stress is given by

$$\gamma_{sf} = -\frac{k_BT}{4\Delta A}\left[\ln\left\langle \exp\left(-\frac{\Delta U^+}{k_BT}\right)\right\rangle - \ln\left\langle \exp\left(-\frac{\Delta U^-}{k_BT}\right)\right\rangle\right] - \frac{L_{z,s}}{2}\left[\frac{1}{2}(\sigma_{xx}+\sigma_{yy}) - \sigma_{zz}\right] \tag{12}$$

The last term on the right side of eqs 10 to 12 represents the effect of solid deformation, which is zero in fluids as stated above.

2.2. Molecular Dynamics Simulations. In this work, we use the LJ solid and fluid model to demonstrate the implementation of the proposed method. In the LJ model, the interaction between two particles α and β is given by

$$U(r_{\alpha\beta}) = 4\varepsilon_{\alpha\beta}\left[\left(\frac{\sigma_{\alpha\beta}}{r_{\alpha\beta}}\right)^{12} - \left(\frac{\sigma_{\alpha\beta}}{r_{\alpha\beta}}\right)^{6}\right] \tag{13}$$

where $r_{\alpha\beta}$ is the distance between particle α and β, and $\varepsilon_{\alpha\beta}$ and $\sigma_{\alpha\beta}$ are energy and size parameters, respectively. Note that $\varepsilon_{\alpha\beta}$ and $\sigma_{\alpha\beta}$ are different from ε_{ij} and σ_{ij} in eq 8 which can be distinguished by the subscripts. We use the subscripts ss, ff, and sf to denote the interaction between solid−solid, fluid−fluid, and solid−fluid particles, respectively. All the quantities are given in reduced units. The dimensionless parameters are presented in Table S1. The simulations are performed using the Large-scale Atomic/Molecular Massively Parallel Simulator (LAMMPS).[39] The molecular structures are rendered with Visual Molecular Dynamics (VMD).[40]

The solid phase consists of 10 × 10 × 10 face-centered-cubic (fcc) unit cells and contains 4200 particles (see Figure 2a). The fluid phase consists of 3000 particles. The periodic boundary condition is applied to all three directions. The mass m^* and size parameter σ^* are set to 1 for both phases. A cutoff distance of 3.0 is employed, where the LJ potential is shifted to 0. The energy parameter ε_{ff} for fluid is 1. ε_{ss} is set to 16 to maintain the structure of the solid, while ε_{sf} is set to 1.2 and 4.0 to represent weak and strong solid−fluid interactions, respectively. The temperature ranges from 0.8 to 1.2, and pressure in the z-direction varies from 0.1 to 1.5. The values are selected to ensure the two-phase coexistence and cover a similar range in the literature.[36] For each condition, the system is initialized with an NpT ensemble for 4×10^6 steps and then switched to an Np_zT ensemble for 2×10^6 steps.[27] The time step is 0.005. In an Np_zT ensemble, the dimensions in the x- and y-directions are kept constant; the dimension in the z-direction is allowed to change. The pressure in the z-direction is kept constant using the Parrinello−Rahman barostat.[41] The Nosé−Hoover thermostat

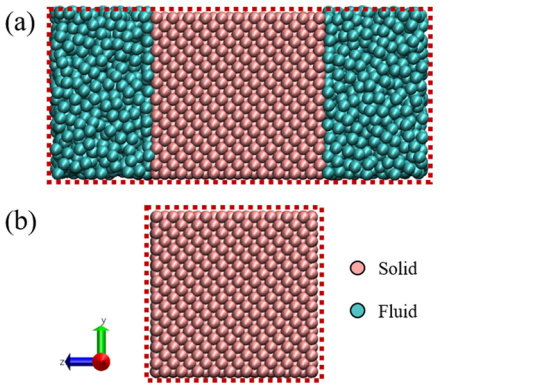

Figure 2. Configuration of the solid−fluid system and the corresponding bulk solid phase for stress calculation. (a) 4200 solid (10 × 10 × 10 fcc cells) and 3000 fluid particles. (b) 4000 solid particles (10 × 10 × 10 fcc cells). The extra 200 solid particles in panel (a) compared to that in panel (b) is to keep the solid structure symmetrical in the z-direction.

https://doi.org/10.1021/acs.jpca.1c00735
J. Phys. Chem. A 2021, 125, 5841−5848

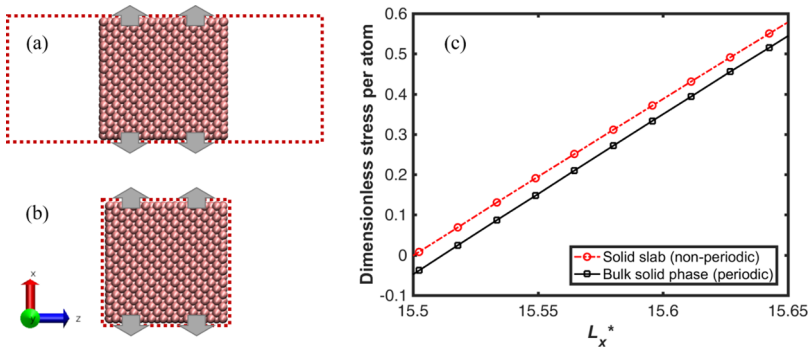

Figure 3. Sketch for surface tension calculation. (a) Solid−vacuum system with a nonperiodic boundary. (b) Bulk solid phase with a periodic boundary. (c) Difference of stress per atom under tension between the two models in (a) and (b).

is applied.[42,43] The damping parameters for barostat and thermostat are both 0.5. The length of the Nosé−Hoover chain is 3. The three directions are independent in the NpT simulations. Then, we perform a second round of simulations using the NpT ensemble (1×10^6 steps) and then the Np_zT ensemble (1×10^6) to investigate equilibration in the dimensions, temperature, and pressure. Another 1×10^6 steps in the Np_zT ensemble are performed to collect the data.

We have also carried out the simulations for the solid phase in vacuum without the fluid phase. The system has the same size ($10 \times 10 \times 10$ cells) as the model given in Figure 2a but without fluids. The volume of the void space is about $15.5 \times 15.5 \times 19.0$ in order to avoid the interaction across the periodic boundary in the z-direction. The simulations are conducted in an NVT ensemble with 2×10^6 steps for relaxation and 1×10^6 steps for data production.

In calculations of interfacial energy, each snapshot from the molecular dynamics (MD) simulations is analyzed by the free-energy perturbation method. The interfacial free energy is calculated based on the working expression in terms of stress in eq 12. The first term in eq 12 is estimated based on the average of 1000 snapshots. The ratio $\Delta A/A$ is set to 0.0001 in this study. The stress of the solid phase in the second term is analyzed through an independent simulation for the bulk solid phase (Figure 2b). The purpose of performing the independent simulation is mainly to avoid the effect of the interfacial tension on the bulk solid phase, which helps avoid the complexities of local stress calculation in a subregion of the whole system. The bulk solid phase has exactly the same dimension as in the two-phase system (Figure 2a) in the x- and y-directions. The size in the z-direction is close to the thickness of the solid slab, as shown in Figure 2a. For this particular case, the bulk solid phase given in Figure 2b has $10 \times 10 \times 10$ cells (4000 atoms). The pressure in the z-direction is controlled by a barostat using the same setting as mentioned before. We performed 1×10^6 steps for relaxation and another 1×10^6 steps for stress calculation.

The Np_zT simulation starts from the last step of the NpT simulation, where the cross-sectional area has randomness. For example, the mean dimension in the x-direction of the system in Figure 2a is 15.5018, and the standard deviation is 0.0086 based on 1 ns simulation. Because the dimensions in the x- and y-directions are kept constant in the Np_zT ensemble, the stress in the solid phase has minor deviations from the average stress over the NpT step. There is also a difference in stress between the tangential and normal directions to the interface. For each condition, we apply an additional strain of ±0.5% from the original condition along either the x- or y-direction to further examine the effect of deformation, in which the displacement is about ±0.08. In general, stress is sensitive to strain in solids. Equation 12 shows that the accuracy of the interfacial free energy can be affected by $L_{z,s}$. We perform simulations at different conditions of solid deformation. The interfacial free energy can be determined by fitting the following function

$$\gamma_{TA} = \gamma_{sf} + \frac{L_{z,s}}{2}\Delta\sigma \tag{14}$$

where γ_{TA} represents the first term on the right side of eq 12 from the conventional test area method. The term $\Delta\sigma = (\sigma_{xx} + \sigma_{yy})/2 - \sigma_{zz}$ is the deviatoric stress representing the stress difference between the tangential and normal directions to the interface. The deviatoric stress $\Delta\sigma$ is obtained by the simulations using the bulk solid phase in Figure 2b. The interfacial free energy γ_{sf} is calculated from the intercept. The error bars are based on the 95% confidence interval of the fitting. An example is presented in Figure S1.

2.3. Validation. To validate the method, we perform two types of simulations: surface tension of the solid−vacuum system and size dependency examination for the solid−fluid system.

We use direct stretching of a solid slab and the bulk solid phase (see Figure 3). A quasi-static extension in the x-direction is simulated.[44,45] The NVT simulation is performed for the solid slab, while an Np_zT simulation is carried out for the bulk solid phase. The dimensions in the x- and y-directions for the bulk solid phase are kept the same as in the solid−vacuum model. The pressure in the z-direction is set to 0. Ten stages are simulated for each model, where the strain of each stage is 0.001. The temperature is set to 1.0. In each stage, we carry out 1×10^5 steps for relaxation and another 1×10^5 steps for data collection. We may assume that the stress difference between the two systems is fully contributed by the surface tension. Then, the surface tension can be estimated based on

$$\tau = \frac{(p^*_{x,\text{slab}} - p^*_{x,\text{bulk}})N_{\text{slab}}}{2L_y} \tag{15}$$

where $p^*_{x,\text{slab}}$ and $p^*_{x,\text{bulk}}$ are the stress per atom of the solid slab and the bulk solid phase, respectively. N_{slab} is the number of atoms of the solid slab. The calculated surface tension is 5.92 ± 0.26, and the surface free energy based on the proposed method is 6.01 ± 0.09. The error bar of the surface tension is obtained based on the standard deviation from the results within the strain of 0.5%. The relationship between surface free energy and surface tension for solids is described by the Shuttleworth

https://doi.org/10.1021/acs.jpca.1c00735
J. Phys. Chem. A 2021, 125, 5841−5848

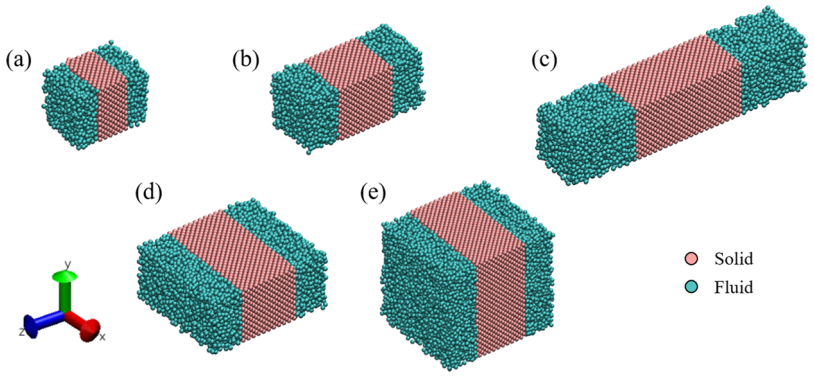

Figure 4. Configurations of the solid–fluid systems for the examination of size dependency. The size and number of particles are listed in Table 1.

equation $\left(\tau = \gamma + \frac{\partial \gamma}{\partial A}\right)$.[46,47] Surface tension at unstrained or low-strain conditions is equal to the surface energy. The validity of the Shuttleworth equation at high strain is under debate.[47] In our simulations, the surface tension and surface free energy are close. It implies that the second term in the Shuttleworth equation may be negligible for small strains.

The size dependency is examined based on five different sizes (see Figure 4). The corresponding size and number of atoms are listed in Table 1. The error bars are based on the 95% confidence interval of the fitting. The conditions are as follows: $T^* = 1.0$, $p_z^* = 0.1$, and $\varepsilon_{sf} = 1.2$. The results show that the solid–fluid interfacial free energy is nearly independent of size in the proposed method. The variation among these systems may be mainly from the inherent uncertainty of MD simulations.

Table 1. Interfacial Free Energy Based on Different Sizes of the System

no.	solid (cells)	number of particles (solid)	number of particles (fluid)	interfacial energy
(a)	10 × 10 × 5	2200	2000	5.73 ± 0.13
(b)	10 × 10 × 10	4200	3000	5.77 ± 0.17
(c)	10 × 10 × 20	8200	6000	6.00 ± 0.30
(d)	10 × 20 × 10	8400	6000	5.80 ± 0.09
(e)	10 × 40 × 10	16,800	12,000	5.84 ± 0.02

3. RESULTS AND DISCUSSION

A comparison of the calculated interfacial free energy based on the conventional test area and our proposed method is presented in Figure 5. The results reveal that there is a significant difference between the two methods at different temperatures and pressures. Without consideration of deformation (the conventional test area method), the calculated interfacial free energy can be either positive or negative, depending on the stress condition. The negative values are unphysical and in violation of thermodynamic stability. The γ_{TA} from the test area method, without consideration of deformation, may not have the correct trend with respect to temperature and pressure.

The first term in eq 12, γ_{TA}, represents the conventional test area method. The second term is the contribution from solid deformation. The contribution of each term in eq 12 under various stress conditions is presented in Figure 6. The results based on high $\Delta\sigma$ may give a clear picture. The higher deviatoric stress $\Delta\sigma$ is obtained by performing an additional deformation ($\pm$0.5%) in the x- or y-direction from the original conditions in the MD simulations shown in Figure 2a. With higher $\Delta\sigma$, γ_{TA} from the test area method deviates more from γ_{sf}. Higher tension in the x- or y-direction results in much higher γ_{TA}, which has positive deviatoric stress $\Delta\sigma$ in eq 14. If $\Delta\sigma$ is positive, which implies a net tension along the plane of the interface, the net effect of stress is in the same direction as the interfacial tension. The test area method may overestimate the interfacial energy. Otherwise, the net effect is along the opposite direction to the interfacial tension due to negative $\Delta\sigma$. In such a condition, high compression leads to negative values. The contributions of the second term are much less under low-stress conditions. The contribution of solid deformation can only be zero if $(\sigma_{xx} + \sigma_{yy})/2 = \sigma_{zz}$ or $(\varepsilon_{xx} + \varepsilon_{yy})/2 = \varepsilon_{zz}$. It is difficult to control the stress (σ_{xx} and σ_{yy}) in the solid phase independently in the Np_zT

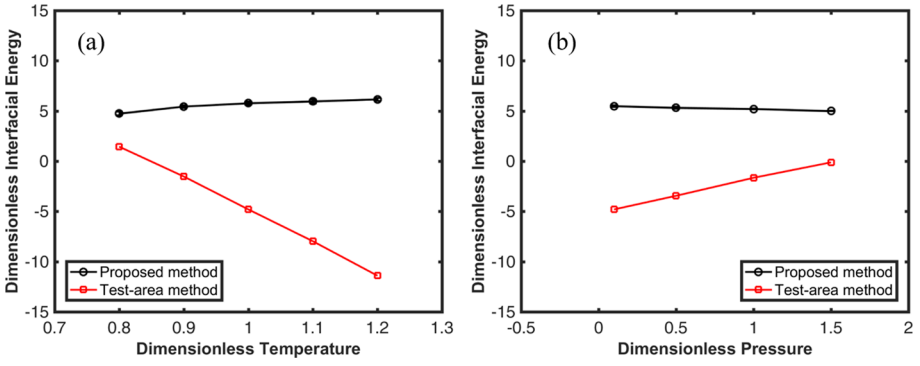

Figure 5. Interfacial free energy vs temperature and pressure in the z-direction from the conventional test area method and the proposed method. (a) $p_z^* = 0.1$; $\varepsilon_{sf} = 1.2$. (b) $T^* = 1.0$; $\varepsilon_{sf} = 1.2$.

https://doi.org/10.1021/acs.jpca.1c00735
J. Phys. Chem. A 2021, 125, 5841−5848

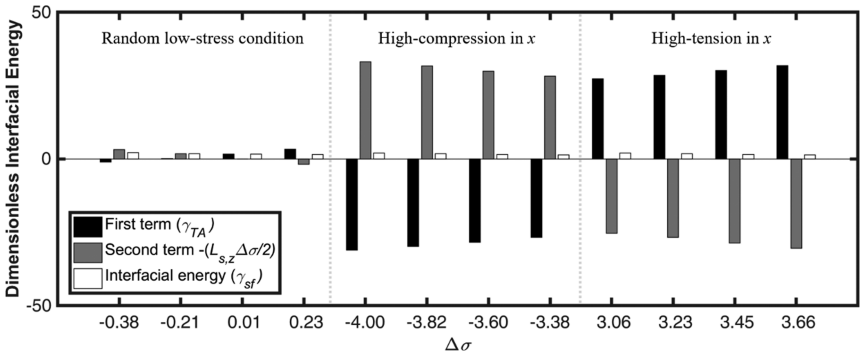

Figure 6. Contribution of the two terms in eq 12. $p_z^* = 0.1$; $T^* = 1.0$; $\varepsilon_{sf} = 1.2$.

ensemble because the dimensions in the *x*- and *y*-directions are kept constant (see Figure S2).

Solid−fluid interactions are represented by the energy parameter ε_{sf}. To examine the effect of ε_{sf} on interfacial energy, we perform simulations with ε_{sf} of 1.2 and 4.0. The results in Figure 7 reveal that ε_{sf} may change the trend of interfacial free

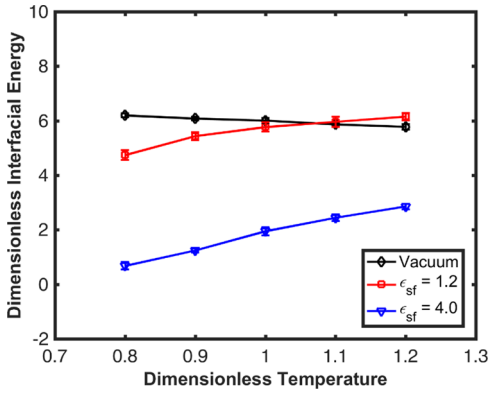

Figure 7. Interfacial and surface free energy vs temperature for solid−vacuum and solid−fluid systems. The pressure p_z^* is 0.1 for solid−fluid systems. The error bars are based on the 95% confidence interval of the fitting, which is smaller than the symbols.

energy with respect to temperature. This effect is related to adsorption. For the solid phase, as temperature increases, the particles in the solid vibrate more, and the cohesion decreases. The surface free energy decreases with temperature increase accordingly. The thickness $L_{z,s}$ of the solid slab can be estimated from eq 14. The mean thickness of the simulations shown in Figure 7 is 16.566 with a standard deviation of 0.038.

Higher ε_{sf} generally results in stronger adsorption. In weak adsorption ($\varepsilon_{sf} = 1.2$), the interfacial free energy is close to the solid−vacuum surface free energy. There is an appreciable reduction at relatively low temperatures due to adsorption. In strong adsorption ($\varepsilon_{sf} = 4.0$), the interfacial free energy is reduced significantly. In both cases, as the temperature increases, the adsorption decreases. Then, the interfacial free energy increases as temperature increases, which approaches the solid−vacuum surface free energy at high temperature. Overall, adsorption is a key parameter in the lowering of interfacial energy.

4. CONCLUSIONS

The main conclusions drawn from this study are as follows:

(1) The incorporation of solid deformation in the expression for Helmholtz free energy is to compute the surface free energy and interfacial free energy density from the free-energy perturbation method. Our results demonstrate a significant effect from solid deformation in the calculated interfacial free energy.

(2) The size dependency of the proposed method is low as expected.

(3) The interfacial free energy density calculated from the conventional test area method without solid deformation contribution may lead to unphysical results.

(4) Adsorption has a pronounced effect on solid−fluid interfacial energy. In weak adsorption, the interfacial free energy is close to the solid−vacuum surface free energy. Strong adsorption results in a significant reduction in interfacial energy. As the temperature increases, the adsorption decreases, and the interfacial free energy increases.

A key conclusion from this work is that different fluids may have a significant effect on the interfacial free energy density due to adsorption. Because interfacial free energy density affects the mechanical stability of deformable materials, fluids with significant adsorption reduce the toughness of these materials.

This work establishes a working expression that can be used in molecular simulations for the interfacial free energy of solid−fluid systems with various industrial and technological applications.

■ ASSOCIATED CONTENT

Supporting Information

The Supporting Information is available free of charge at https://pubs.acs.org/doi/10.1021/acs.jpca.1c00735.

Definition of the dimensionless parameters; interfacial free energy based on eq 14; sketch of the nonuniform stress in the Np_zT ensemble; and thermodynamics of the perturbation on solid−fluid systems (PDF)

■ AUTHOR INFORMATION

Corresponding Author

Abbas Firoozabadi − *Department of Chemical and Biomolecular Engineering, Rice University, Houston, Texas 70057, United States; Reservoir Engineering Research Institute, Palo Alto, California 94301, United States;* orcid.org/0000-0001-6102-9534; Email: abbas.firoozabadi@rice.edu

https://doi.org/10.1021/acs.jpca.1c00735
J. Phys. Chem. A 2021, 125, 5841−5848

Author

Tianhao Wu − *Department of Chemical and Biomolecular Engineering, Rice University, Houston, Texas 70057, United States; Reservoir Engineering Research Institute, Palo Alto, California 94301, United States*

Complete contact information is available at: https://pubs.acs.org/10.1021/acs.jpca.1c00735

Notes

The authors declare no competing financial interest.

■ ACKNOWLEDGMENTS

This work is partially supported by the member companies of the Reservoir Engineering Research Institute (RERI). The ExxonMobil project on CO_2 fracking at Rice University under Agreement #EM11539 also provided funding. The support is appreciated.

■ REFERENCES

(1) Firoozabadi, A. *Thermodynamics and Applications in Hydrocarbon Energy Production*; McGraw-Hill Education, 2016.

(2) Bailey, A. I.; Kay, S. M. A. Direct Measurement of the Influence of Vapour, of Liquid and of Oriented Monolayers on the Interfacial Energy of Mica. *Proc. R. Soc. Lond. Ser. A Math. Phys. Sci.* **1967**, *301*, 47−56.

(3) Parks, G. A. Surface and Interfacial Free Energies of Quartz. *J. Geophys. Res.: Solid Earth* **1984**, *89*, 3997−4008.

(4) Jiang, H.; Müller-Plathe, F.; Panagiotopoulos, A. Z. Contact Angles from Young's Equation in Molecular Dynamics Simulations. *J. Chem. Phys.* **2017**, *147*, No. 084708.

(5) Middleton, R. S.; Carey, J. W.; Currier, R. P.; Hyman, J. D.; Kang, Q.; Karra, S.; Jiménez-Martínez, J.; Porter, M. L.; Viswanathan, H. S. Shale Gas and Non-Aqueous Fracturing Fluids: Opportunities and Challenges for Supercritical CO2. *Appl. Energy* **2015**, *147*, 500−509.

(6) Gandossi, L. An Overview of Hydraulic Fracturing and Other Formation Stimulation Technologies for Shale Gas Production. *Eur. Commission Jt. Res. Cent. Tech.Rep.* **2013**, 26347.

(7) Liu, H.; Wang, F.; Zhang, J.; Meng, S.; Duan, Y. Fracturing with Carbon Dioxide: Application Status and Development Trend. *Pet. Explor. Dev.* **2014**, *41*, 513−519.

(8) Sinal, M. L.; Lancaster, G. Liquid CO2 Fracturing: Advantages and Limitations. *J. Can. Pet. Technol.* **1987**, *26*, 26−30.

(9) Wu, T.; Zhao, J.; Zhang, W.; Zhang, D. Nanopore Structure and Nanomechanical Properties of Organic-Rich Terrestrial Shale: An Insight into Technical Issues for Hydrocarbon Production. *Nano Energy* **2020**, *69*, No. 104426.

(10) Lyu, Q.; Long, X.; Ranjith, P. G.; Tan, J.; Kang, Y.; Wang, Z. Experimental Investigation on the Mechanical Properties of a Low-Clay Shale with Different Adsorption Times in Sub-/Super-Critical CO2. *Energy* **2018**, *147*, 1288−1298.

(11) Al-Ameri, W. A.; Abdulraheem, A.; Mahmoud, M. Long-Term Effects of CO2 Sequestration on Rock Mechanical Properties. *J. Energy Resour. Technol.* **2016**, *138*, No. 012201.

(12) Yin, H.; Zhou, J.; Xian, X.; Jiang, Y.; Lu, Z.; Tan, J.; Liu, G. Experimental Study of the Effects of Sub-and Super-Critical CO2 Saturation on the Mechanical Characteristics of Organic-Rich Shales. *Energy* **2017**, *132*, 84−95.

(13) Perera, M. S. A.; Ranjith, P. G.; Viete, D. R. Effects of Gaseous and Super-Critical Carbon Dioxide Saturation on the Mechanical Properties of Bituminous Coal from the Southern Sydney Basin. *Appl. Energy* **2013**, *110*, 73−81.

(14) Lu, Y.; Chen, X.; Tang, J.; Li, H.; Zhou, L.; Han, S.; Ge, Z.; Xia, B.; Shen, H.; Zhang, J. Relationship between Pore Structure and Mechanical Properties of Shale on Supercritical Carbon Dioxide Saturation. *Energy* **2019**, *172*, 270−285.

(15) Wang, S.; Liu, K.; Han, J.; Ling, K.; Wang, H.; Jia, B. Investigation of Properties Alternation During Super-Critical CO2 Injection in Shale. *Appl. Sci.* **2019**, *9*, 1686.

(16) Sun, Z.; Espinoza, D. N.; Balhoff, M. T.; Dewers, T. A. Discrete Element Modeling of Micro-Scratch Tests: Investigation of Mechanisms of CO2 Alteration in Reservoir Rocks. *Rock Mech. Rock Eng.* **2017**, *50*, 3337−3348.

(17) Sun, Z.; Espinoza, D. N.; Balhoff, M. T. Discrete Element Modeling of Indentation Tests to Investigate Mechanisms of CO2-Related Chemomechanical Rock Alteration. *J. Geophys. Res.: Solid Earth* **2016**, *121*, 7867−7881.

(18) Anderson, T. L. *Fracture Mechanics: Fundamentals and Applications*; CRC Press: Boca Raton, 2005.

(19) Irwin, G. R. Analysis of Stresses and Strains near the End of a Crack Traversing a Plate. *J. Appl. Mech.* **1957**, *24*, 361−364.

(20) Heider, Y.; Reiche, S.; Siebert, P.; Markert, B. Modeling of Hydraulic Fracturing Using a Porous-Media Phase-Field Approach with Reference to Experimental Data. *Eng. Fract. Mech.* **2018**, *202*, 116−134.

(21) Zhou, S.; Zhuang, X.; Rabczuk, T. Phase-Field Modeling of Fluid-Driven Dynamic Cracking in Porous Media. *Comput. Methods Appl. Mech. Eng.* **2019**, *350*, 169−198.

(22) Griffith, A.; Vi, A. The Phenomena of Rupture and Flow in Solids. *Philos. Trans. R. Soc., A* **1921**, *221*, 163−198.

(23) Griffith, A. A. *The Theory of Rupture. In* Proceedings of the First International Congress for Applied Mechanics, 1924; 55−63, DOI: 10.1201/9781420058215.

(24) Irwin, G. R. Fracture Dynamics. In *Fracturing of Metals*; ASM, Cleveland, 1948; 147−166 DOI: 10.1201/9781420058215.

(25) Irwin, G. R. Fracture. In *Elasticity and Plasticity/Elastizität Und Plastizität*; Flügge, S., Ed. Springer: Berlin, Heidelberg, 1958; 551−590 DOI: 10.1201/9781420058215.

(26) Kirkwood, J. G.; Buff, F. P. The Statistical Mechanical Theory of Surface Tension. *J. Chem. Phys.* **1949**, *17*, 338−343.

(27) Kunieda, M.; Nakaoka, K.; Liang, Y.; Miranda, C. R.; Ueda, A.; Takahashi, S.; Okabe, H.; Matsuoka, T. Self-Accumulation of Aromatics at the Oil−Water Interface through Weak Hydrogen Bonding. *J. Am. Chem. Soc.* **2010**, *132*, 18281−18286.

(28) Gloor, G. J.; Jackson, G.; Blas, F. J.; de Miguel, E. Test-Area Simulation Method for the Direct Determination of the Interfacial Tension of Systems with Continuous or Discontinuous Potentials. *J. Chem. Phys.* **2005**, *123*, 134703.

(29) Zwanzig, R. W. High-Temperature Equation of State by a Perturbation Method I. Nonpolar Gases. *J. Chem. Phys.* **1954**, *22*, 1420−1426.

(30) Leroy, F.; dos Santos, D. J. V. A.; Müller-Plathe, F. Interfacial Excess Free Energies of Solid−Liquid Interfaces by Molecular Dynamics Simulation and Thermodynamic Integration. *Macromol. Rapid Commun.* **2009**, *30*, 864−870.

(31) Qi, X.; Zhou, Y.; Fichthorn, K. A. Obtaining the Solid-Liquid Interfacial Free Energy via Multi-Scheme Thermodynamic Integration: Ag-Ethylene Glycol Interfaces. *J. Chem. Phys.* **2016**, *145*, 194108.

(32) Davidchack, R. L.; Laird, B. B. Direct Calculation of the Crystal−Melt Interfacial Free Energies for Continuous Potentials: Application to the Lennard-Jones System. *J. Chem. Phys.* **2003**, *118*, 7651−7657.

(33) Qi, X.; Fichthorn, K. A. Theory of the Thermodynamic Influence of Solution-Phase Additives in Shape-Controlled Nanocrystal Synthesis. *Nanoscale* **2017**, *9*, 15635−15642.

(34) Leroy, F.; Müller-Plathe, F. Dry-Surface Simulation Method for the Determination of the Work of Adhesion of Solid−Liquid Interfaces. *Langmuir* **2015**, *31*, 8335−8345.

(35) Iglauer, S.; Mathew, M. S.; Bresme, F. Molecular Dynamics Computations of Brine−CO2 Interfacial Tensions and Brine−CO2−Quartz Contact Angles and Their Effects on Structural and Residual Trapping Mechanisms in Carbon Geo-Sequestration. *J. Colloid Interface Sci.* **2012**, *386*, 405−414.

(36) Nair, A. R.; Sathian, S. P. A Molecular Dynamics Study to Determine the Solid-Liquid Interfacial Tension Using Test Area Simulation Method (TASM). *J. Chem. Phys.* **2012**, *137*, No. 084702.

(37) Alhosani, M.; Valiya Parambathu, A.; Yrazu, F. M.; Asthagiri, D.; Chapman, W. *Dissecting the Salinity-Dependence of Wettability in Oil/Brine/Calcite System Using Molecular Simulations*. Energy. 2019, DOI: 10.26434/chemrxiv.11462088.v1.
(38) d'Oliveira, H. D.; Davoy, X.; Arche, E.; Malfreyt, P.; Ghoufi, A. Test-Area Surface Tension Calculation of the Graphene-Methane Interface: Fluctuations and Commensurability. *J. Chem. Phys.* **2017**, *146*, 214112.
(39) Plimpton, S. Fast Parallel Algorithms for Short-Range Molecular Dynamics. *J. Comput. Phys.* **1995**, *117*, 1−19.
(40) Humphrey, W.; Dalke, A.; Schulten, K. VMD: Visual Molecular Dynamics. *J. Mol. Graph.* **1996**, *14*, 33−38.
(41) Martyna, G. J.; Tobias, D. J.; Klein, M. L. Constant Pressure Molecular Dynamics Algorithms. *J. Chem. Phys.* **1994**, *101*, 4177−4189.
(42) Nosé, S. A Unified Formulation of the Constant Temperature Molecular Dynamics Methods. *J. Chem. Phys.* **1984**, *81*, 511−519.
(43) Hoover, W. G. Canonical Dynamics: Equilibrium Phase-Space Distributions. *Phys. Rev. A* **1985**, *31*, 1695−1697.
(44) Wu, T.; Firoozabadi, A. Mechanical Properties and Failure Envelope of Kerogen Matrix by Molecular Dynamics Simulations. *J. Phys. Chem. C* **2020**, *124*, 2289−2294.
(45) Wu, T.; Firoozabadi, A. Fracture Toughness and Surface Energy Density of Kerogen by Molecular Dynamics Simulations in Tensile Failure. *J. Phys. Chem. C* **2020**, *124*, 15895−15901.
(46) Shuttleworth, R. The Surface Tension of Solids. *Proc. Phys. Soc. Sect. A* **1950**, *63*, 444.
(47) Pasquale, N. D.; Davidchack, R. L. Shuttleworth Equation: A Molecular Simulations Perspective. *J. Chem. Phys.* **2020**, *153*, 154705.

https://doi.org/10.1021/acs.jpca.1c00735
J. Phys. Chem. A 2021, 125, 5841−5848